ELSEVIER

Contents lists available at ScienceDirect

Remote Sensing of Environment

journal homepage: www.elsevier.com/locate/rse



A multi-sensor, multi-scale approach to mapping tree mortality in woodland ecosystems



Michael J. Campbell^{a,*}, Philip E. Dennison^b, Jesse W. Tune^c, Steven A. Kannenberg^d, Kelly L. Kerr^d, Brian F. Codding^e, William R.L. Anderegg^d

- ^a Department of Geosciences, Fort Lewis College, 1000 Rim Drive, Durango, CO 81301, USA
- b Department of Geography, University of Utah, 260 Central Campus Drive, Salt Lake City, UT 84112, USA
- ^c Department of Anthropology, Fort Lewis College, 1000 Rim Drive, Durango, CO 81301, USA
- ^d School of Biological Sciences, University of Utah, 257 South 1400 East, Salt Lake City, UT 84112, USA
- ^e Department of Anthropology, University of Utah, 260 Central Campus Drive, Salt Lake City, UT 84112, USA

ARTICLE INFO

Keywords: Woodland Pinyon Piñon Juniper Land cover change Tree mortality Drone UAV UAS Lidar

Landsat

ABSTRACT

Woodland ecosystems, dominant on nearly 4% of all terrestrial land globally, are faced with a variety of threats, including increasingly prolonged and severe droughts, invasive insect outbreaks, and the rapid spread of pathogens. While many remote sensing methods have been developed for the detection and quantification of mortality in forested environments, woodland ecosystems present unique challenges to accurately mapping tree die-off due to relatively lower canopy covers, smaller and irregularly-shaped tree crowns, and greater influence of understory vegetation and soil cover on reflectance. To address these challenges, we developed a multi-sensor, multi-scale approach combining the analytical strengths of centimeter-resolution unmanned aerial system imagery for interpreting individual tree-level mortality, airborne lidar for crown mapping and quantifying percent canopy mortality, and Landsat imagery for upscaling mortality estimates to a regional scale. This approach utilizes a new algorithm for delineating the shapes of small, irregular woodland tree crowns using lidar. To demonstrate the application of this method, we map the extent and severity of a recent tree mortality event in piñon-juniper (PJ) woodlands of southeastern Utah. Our results suggest that 39% of PJ in this region has experienced some level of mortality, with patches exceeding 50% mortality. An analysis of potential mortality drivers revealed that canopy cover, terrain, and recent winter precipitation conditions are most directly linked with mortality, although the explanatory power of the mortality driver model was low. Our approach demonstrates a methodology that could be used for tree mortality mapping and scaling in a variety woodland ecosystems, and can provide a strong basis for further ecophysiological, ecological, and carbon cycle studies involving woodland tree mortality.

1. Introduction

Woodland ecosystems are widely distributed throughout the world, often found in semiarid regions where precipitation totals are sufficient to support some arboreal vegetation, yet insufficient to promote a high density of trees. Although specific definitions can vary, woodland ecosystems are generally considered to be areas that possess low-to-moderate tree cover, existing on a spectrum between forest ecosystems, with relatively high tree cover, and savanna ecosystems, with relatively low tree cover (Ratnam et al., 2011; Taft, 1997). Open-canopy dryland woodland ecosystems with canopy covers between 10% and 40%

dominate on approximately 550 Mha globally (nearly 4% of all terrestrial land), spanning every continent besides Antarctica (Bastin et al., 2017). Semiarid ecosystems are one of the major drivers of interannual variability in the global land carbon sink, and thus their response to climate plays a critical role in the Earth system (Ahlström et al., 2015). Although woodland trees may be well-adapted to the semiarid conditions in which they dominate, changes in the frequency, length, and severity of drought events linked to climate change place woodland ecosystems at particular risk in the decades to come (Clifford et al., 2011; Matusick et al., 2012). In order to enhance our understanding of how woodland environments may respond to projected climatic

E-mail addresses: mcampbell@fortlewis.edu (M.J. Campbell), dennison@geog.utah.edu (P.E. Dennison), jwtune@fortlewis.edu (J.W. Tune), s.kannenberg@utah.edu (S.A. Kannenberg), kelly.kerr@utah.edu (K.L. Kerr), brian.codding@anthro.utah.edu (B.F. Codding), anderegg@utah.edu (W.R.L. Anderegg).

^{*} Corresponding author.

changes, we need to leverage all of the information and analytical tools at our disposal, including remote sensing (Allen et al., 2015). The unique capacity of remote sensing for providing spatially-explicit maps of tree mortality can provide an invaluable basis for studying potential mortality drivers (Anderegg et al., 2016). Furthermore, regional maps of climate-driven tree mortality are essential tools for improving vegetation models and climate-carbon cycle feedback projections, providing critical validation and benchmarking datasets for poorly-constrained tree mortality algorithms (Hartmann et al., 2018).

Approaches for using remote sensing to quantify tree mortality generally fall into two categories: (1) individual tree-based mortality mapping driven by high spatial resolution data (Clark et al., 2004; Garrity et al., 2013; Guo et al., 2007; Waser et al., 2014); and (2) standlevel mortality mapping driven by moderate spatial resolution data (Bullock et al., 2020; Coops et al., 2009; Fortin et al., 2020; Fraser and Latifovic, 2005; Macomber and Woodcock, 1994; Meigs et al., 2011; Van Gunst et al., 2016). Generally, high spatial resolution data come at the expense of high temporal resolution, due to the opportunistic nature of data capture (e.g. from an aircraft or pointable satellite), and tend to be collected over relatively smaller areas, limiting the ability to determine when morality occurred and its spatial extent. The strengths and weaknesses of the second approach are inverse - the ability to map individual tree-level mortality is compromised in favor of knowing when the mortality occurred and being able to map mortality at a broader spatial scale.

A few studies in higher-cover, forested environments have sought to leverage the benefits of both high and moderate spatial resolution data for mapping tree mortality by fusing individual tree-level mortality mapping with stand-level mortality mapping (Hart and Veblen, 2015; He et al., 2019; Meddens et al., 2013). Meddens et al. (2013) and Hart and Veblen (2015) used a combination of aerial imagery and time-series Landsat satellite imagery to classify various stages of beetle kill in high-altitude mixed conifer forests of Colorado. He et al. (2019) used a combination of high spatial resolution aerial imagery, hyperspectral aerial imagery, and Landsat to map sudden oak death in higher-density chaparral environments of coastal California.

Remote sensing of tree mortality in open-canopy woodland ecosystems poses significant challenges to multiscale approaches that have not been addressed in the previous literature. Within an image pixel, the spectral contribution of tree mortality can be diluted due to relatively small, irregular, and widely-spaced tree canopies (Smith et al., 2019). Understory vegetation, soil, and rock can provide significant or even dominant contributions to spectral measurements at the scale of high spatial resolution imagery used by previous studies. Figure demonstrates how an approach using approximately 3 m spatial resolution imagery that has successfully been applied in a closed-canopy forest (Hart and Veblen, 2015; Meddens et al., 2013) would be severely limited due to the spatial and spectral characteristics of an open-canopy

woodland. Even at 1 m spatial resolution, it is not possible to determine mortality of individual woodland trees (Fig. 1). Accordingly, a new approach is needed to fuse high and moderate spatial resolution imagery for detecting and mapping tree mortality in sparse, open canopy woodlands. Such an approach could provide insight into the extent and severity of mortality events in these critical, widespread, and threatened ecosystems.

The objectives of this study are to 1) Develop a multi-sensor, multiscale approach to mapping tree mortality that is appropriate for sparse, open canopy woodlands in semiarid environments; 2) Demonstrate the application of this multi-sensor, multi-scale approach to a recent mortality event in piñon-juniper (PJ) woodlands in southeastern Utah; and 3) Use the resulting map to relate percent mortality at 30 m scales to environmental drivers of mortality. We introduce a new approach to mapping tree mortality that leverages the benefits of high-resolution unmanned aerial systems (UAS) imagery for use in interpreting tree mortality, lidar for use in delineating individual tree crowns and quantifying proportional mortality cover, and Landsat imagery for scaling up mortality estimates to a broad spatial scale. As in Meddens and Hicke (2014), our method results in a Landsat pixel-level quantification of percent mortality using relative canopy mortality (RCM), rather than a categorical label (e.g. "live" vs. "dead"). The resulting mortality map is compared to a range of vegetation, terrain, climate, and soil spatial datasets with the intent of illuminating potential drivers of mortality.

2. Background

Piñon-juniper (PJ) woodlands are one of the most widespread woodland-type ecosystems in the North America, spanning ten southwestern US states and occupying over 178,000 km² of land (Fig. S1). They are characterized by a dominance of one or more species of piñon pine and one or more species of juniper (Table S1). Given their widespread distribution, these ecosystems represent an important source of woody biomass and carbon storage (Huang et al., 2009), they act as valuable habitat for a wide range of animal species (Short and McCulloch, 1977), and they provide firewood for heating homes and cooking food among dependent populations in the region (Samuels and Betancourt, 1982). Recent evidence suggests that a major mortality event is underway in PJ woodlands. In summer 2018, while conducting field work in the region, we observed significant amounts of tree mortality occurring within PJ woodlands in southeastern Utah.

PJ woodland cover has expanded since the 1800s (Clifford et al., 2011; Filippelli et al., 2020; Miller and Rose, 1999). Throughout this time frame, juniper trees in particular have encroached into areas that were historically dominated by grasses and shrubs, due to a variety of factors including reduction in fire frequency, increase in livestock grazing activity, and periods of elevated precipitation totals (Miller and

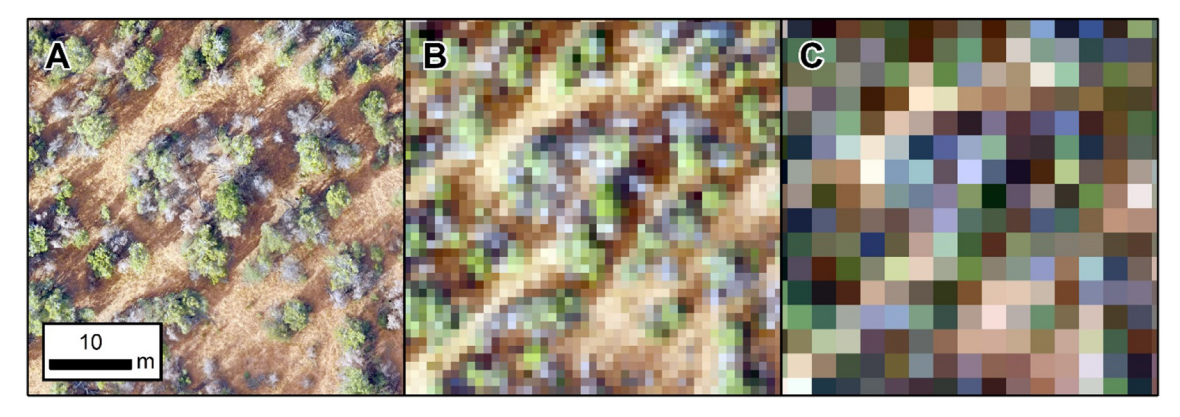


Fig. 1. Comparison between a 4 cm (A), 1 m (B), and 3 m (C) spatial resolution images of a piñon-juniper woodland stand with several dead, predominantly piñon trees.

Rose, 1999). This process can have significant effects on hydrologic and erosional processes, as large lateral root systems of PJ trees outcompete grasses and shrubs, resulting in increased bare soil cover between trees which, in turn, decreases water infiltration, and increases runoff and erosion (Pierson et al., 2010). These changes in ecosystem structure can also alter faunal habitat suitability, including the well-documented effects of decreasing sagebrush steppe extent on threated species such as the greater sage-grouse (*Centrocercus urophasianus*) (Coates et al., 2017)

Although the long-term trend has been one of PJ expansion, episodic periods of drought combined with anomalously-high temperatures in recent years have been linked to widespread PJ mortality in the region (Breshears et al., 2005; Clifford et al., 2013). Mortality can occur directly from the lack of sufficient water to maintain plant water transport and photosynthesis, or more indirectly by increasing susceptibility to attack by pests and/or pathogens (Greenwood and Weisberg, 2008; Shaw et al., 2005). One such major climate-driven mortality event occurred in the 2002-2003 time frame on PJ-dominated landscapes throughout the American Southwest, where vast swaths of piñon pines died off (Shaw et al., 2005). Rates of juniper mortality during that event were negligible by comparison due to their relatively higher drought tolerance (Linton et al., 1998). Particularly in an ecosystem dominated by relatively few tree species such as PJ, major mortality events like these can have dramatic effects on biodiversity (e.g. loss of one or more widespread tree species), ecosystem structure (e.g. shifting from a tree-dominated system to a shrub-dominated system), function (e.g. changes in soil-water interactions), and services (e.g. loss of firewood resources) (Anderegg et al., 2013).

PJ woodlands exist at the edge of the climatic range within which trees can survive in the southwestern US – areas at lower elevations, with higher temperatures, and/or lower annual precipitation totals are dominated by shrubs and grasses, or are lacking vegetation cover altogether (Gori and Bate, 2007). On top of their precarious existence at this critical climatic/environmental threshold, PJ woodlands have experienced significant drought in the last few years. A comparison between recent (2017–2019) monthly temperature and precipitation and long-term (30-year) average monthly temperature and precipitation on CPPJ lands reveals that the majority of recent months have experienced significant drought conditions (Fig. S2).

3. Materials and methods

3.1. Study area

This study is focused on PJ lands in San Juan County (SJC), Utah, USA (Fig. 2). This area was chosen for a few reasons: (1) there is an abundance of PJ vegetation type within this region; (2) it is situated within the core of the PJ range, suggesting that it may be representative of mortality conditions occurring within the broader distribution of this vegetation type; (3) this is where the PJ mortality was first observed in summer, 2018; and (4) airborne lidar data were captured over this area in summer, 2018. SJC is a large county, totaling 20,537 km² in area (an area larger than the entire US state of New Jersey), that features a wide range of elevations (1115-3880 m), climatic conditions, and vegetation types. According to PRISM 30-year averages, this semiarid county receives a total annual precipitation of between 123 mm at the lower, drier elevations to 1074 mm at the higher, wetter elevations. Average annual temperatures range from 16 °C at the lower, warmer elevations to 2 °C at the higher, cooler elevations. PJ is the most widespread ecosystem in the county, occupying a total area of 5934 km².

3.2. Lidar data

Lidar data were collected prior to the start of obvious mortality by the National Center for Airborne Laser Mapping (NCALM) on June 2nd, 2018. The data were collected in five areas throughout SJC within PJ lands, designed to capture the full elevation range of PJ in this area, from 1654 m to 2762 m (Fig. 3). Lidar data were collected from an airborne platform using an Optech Titan sensor, which emits lidar pulses in three wavelengths: green (532 nm), near infrared (1064 nm), and shortwave infrared (1550 nm). The pulses were emitted at 125 kHz, with a scan angle range of \pm 23°. The nominal flying height was 600 m above ground level at a nominal speed of 72 m/s. In all, 4.9 billion pulses were emitted over a total collection area of 229 km², producing an average pulse density of approximately 21.4 pulses/m². The point cloud data were processed by NCALM in order to classify ground points vs. non-ground points. Ground point three-dimensional positional accuracy was measured using 1358 kinematic GPS check points, which yielded a standard deviation of 0.038 m and a mean error of -0.018 m.

3.3. UAS data

UAS data were collected after the start of the mortality event on October 19th and October 26th, 2019 within the southernmost of the five lidar data collection areas shown in Fig. 3. Data were collected using a DJI Phantom 3 Pro in three areas that were selected opportunistically for their accessibility and known presence of varying levels of PJ mortality. In all, the three data collection areas encompass 83.6 ha in area. Imagery was collected along automated flight path transects preprogramed in Pix4Dcapture (Pix4D S.A., Prilly, Switzerland), with a nominal flying height of 100 m above ground level. Image data were collected using the built-in camera, which captures visible-spectrum (RGB) imagery in 12.4 megapixels. Twenty-one ground control points were captured throughout the three collection areas (south: 8; central: 7; north: 6) using a Trimble Geo7x GPS. Georeferenced orthomosaics at a spatial resolution of 4 cm were generated for each of the three areas from the raw data and the ground control points using Pix4Dmapper software (Pix4D S.A., Prilly, Switzerland). The resulting imagery was further georeferenced to ensure precise alignment with the lidar data by manually placing 30 additional points in each of the three data collection areas, resulting in positional root mean squared errors of 0.50 m (south area), 0.34 m (central area), and 0.37 m (north area). An example subset of the UAS imagery is shown in Fig. 1A.

3.4. Landsat data

Thirty-meter spatial resolution Landsat 8 Operational Land Imagery (OLI) data were acquired for two time frames: (1) October 12th, 2017, before the onset of the mortality event; and (2) October 2nd, 2019, which was the most recent, cloud-free, near-anniversary imagery available at the time of analysis. October images were selected because semiarid environments such as PJ feature low tree canopy cover, and as such the spectral influence from understory vegetation during peak growing season (May-August) can outweigh that of piñon and juniper canopies. Conversely, images captured much later than October feature low sun angles, with high shadowing, and often feature snow cover, all of which could degrade the ability to detect mortality. The solar elevation angles for the 2017 and 2019 images used in this study were 42.1° and 45.6°, respectively. Although these moderate sun angles can produce a relatively high shadow fraction, they are well within the bounds of producing reliable surface reflectance information (US Geological Survey, 2019). In order to cover the majority of SJC, two Landsat tiles were needed (path 36, rows 33 and 34). A very small portion of southwestern SJC was cut off from the extent of Landsat data in path 36, representing only 1.6% of the county's area and less than 0.1% of the total PJ in the county. The data were acquired from the United States Geological Survey (USGS) Earth Resources Observation and Science (EROS) Center, who processed the data from its raw form to surface reflectance using the Land Surface Reflectance Code (LaSRC) algorithm (Vermote et al., 2016). In the interest of mapping changes in vegetation cover resulting from tree mortality between these two time frames, several vegetation indices (VI) were generated for each image

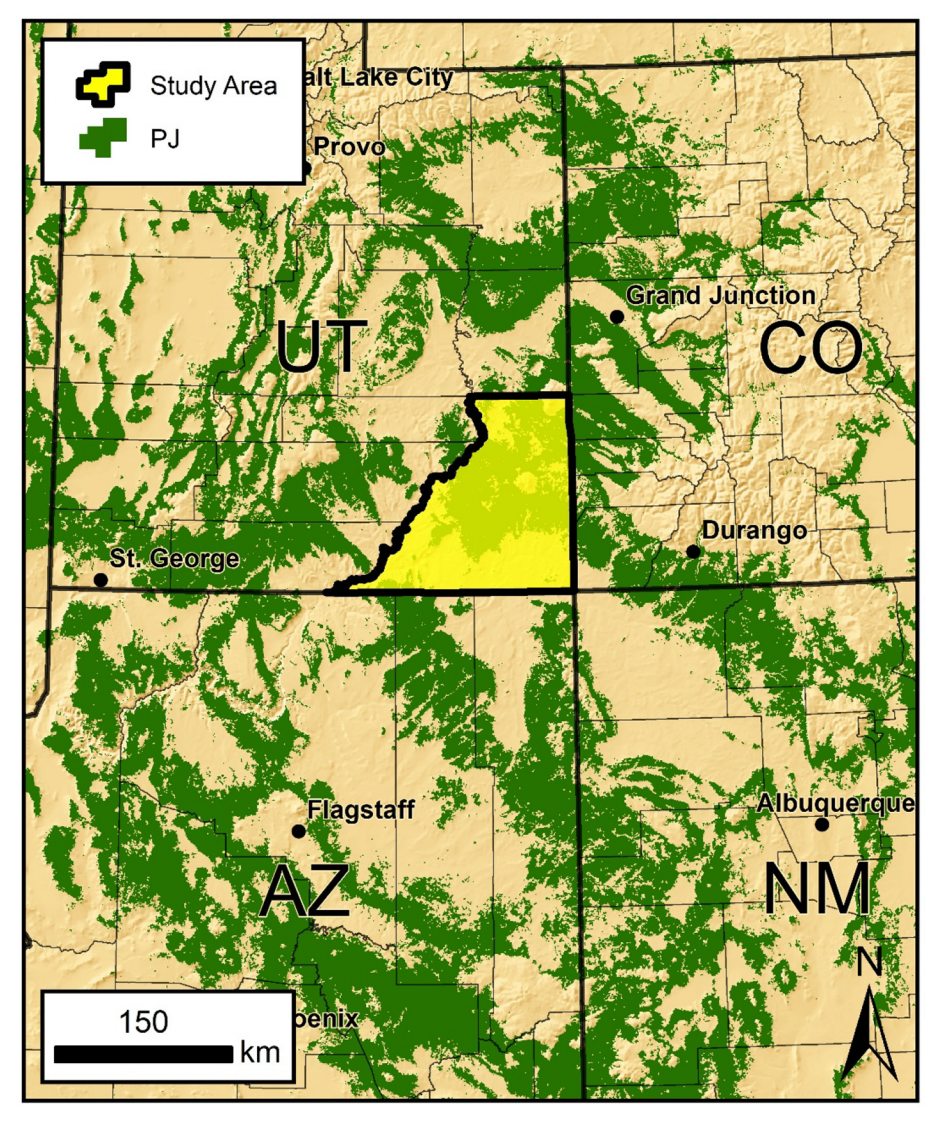


Fig. 2. Map depicting the study area of SJC within the broader range of PJ woodlands throughout the Four Corners region of the US, according to the LANDFIRE existing vegetation type data (Rollins, 2009).

date (Table 1). For each VI, an image difference was calculated between the 2017 and 2019 data.

3.5. Tree crown delineation and reference data creation

The complex structure of piñon and juniper trees do not lend themselves well to most traditional lidar-based tree crown delineation algorithms, which often rely on the assumption that trees come to a single height peak and take a conical or rounded form (Zhen et al., 2016). By comparison, piñon and juniper trees are often multi-stemmed and irregularly-shaped, necessitating a different approach for tree crown delineation. One such effort comes from Krofcheck et al. (2016), but their algorithm does not distinguish between individual trees that overlap one another. Thus, we developed our own algorithm for deriving tree crown polygons from lidar point cloud data, adapted from that of Rahman and Gorte (2009), which relies on point density, rather than point height as a basis of delineation. The method assumes that, even if a tree does not come to a singular high point, the bulk of the biomass within a tree still lies towards its horizontal center point, with decreasing biomass totals as you radiate out from that center point. Based on that assumption we can also assume that lidar pulses will be most likely to interact with the greater density of vegetative surfaces towards the center of the tree, producing a higher lidar point density at the tree's center. The focal sum of lidar points, reflecting the density of points, should then decrease with increasing distance from the center of the tree, and a simple watershed delineation algorithm can be applied to the focal sum to delineate tree crowns.

There are two parameters to consider when employing this algorithm. The first is the minimum height threshold above which points will be counted in the focal sum analysis, and below which they will not (Rahman and Gorte, 2009). The threshold should be selected to eliminate ground points and those that may have reflected off of low-lying, non-tree vegetation surrounding or underneath the tree of interest. For the sake of our study, a height cutoff of 25 cm was selected, since the majority of the understory vegetation in this area is below 25 cm in height. The second parameter to consider when employing this algorithm is the size of the focal window that will be used as a basis for computing the sum of lidar points. If the focal sum window is too small, the resulting sum surface will contain many small peaks, each of which will be delineated as individual tree crowns, resulting in over-segmentation (Fig. 4A). Conversely, if the focal sum window is too large, the resulting sum surface will fail to identify smaller point clusters as they will be consumed by any adjacent, larger point clusters, thus resulting in under-segmentation (Fig. 4D). To resolve the issue of window size sensitivity, we took an average of all of the point sum rasters from 10 cm to 150 cm at an interval of 10 cm to produce an average point

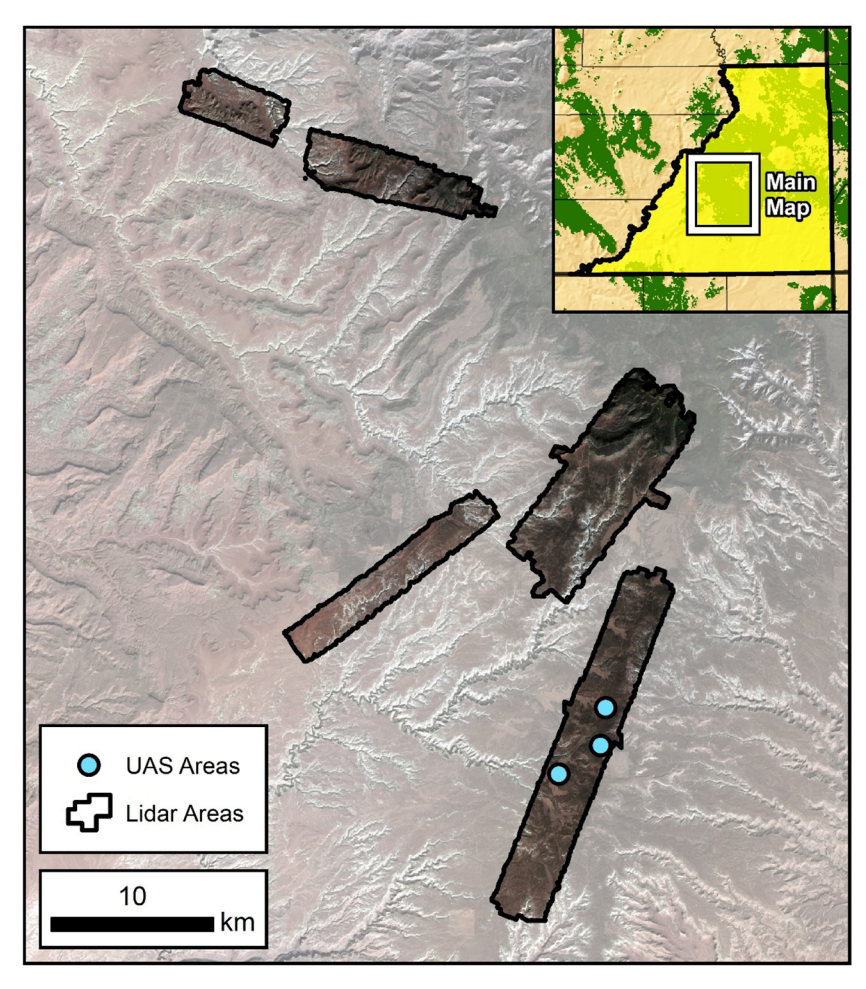


Fig. 3. Map depicting areas within which airborne lidar data were collected on June 2nd, 2018 within SJC. Also shown are points representing the centroids of the three areas (north, central, and south) in which UAS data were collected.

Table 1 VI generated from Landsat 8 OLI imagery for 2017 and 2019 imagery, with abbreviations, formula, and sources. $SWIR_1$ and $SWIR_2$ are Landsat 8 bands 6 and 7, respectively.

Index	Abbreviation	Formula	Source
Normalized Difference Vegetation Index	NDVI	$\frac{(NIR - Red)}{(NIR + Red)}$	Rouse (1974)
Enhanced Vegetation Index	EVI	$2.5 \times \frac{(NIR - Red)}{(NIR + 6 \times Red - 7.5 \times Blue + 1)}$	Liu and Huete (1995)
Near Infrared Reflectance of Vegetation	NIR_V	$NIR \times NDVI$	Badgley et al. (2017)
Soil Adjusted Vegetation Index	SAVI	$1.5 \times \frac{(NIR - Red)}{(NIR + Red + 0.5)}$	Huete (1988)
Modified Soil Adjusted Vegetation Index	MSAVI	$\frac{(2 \times NIR + 1 - \sqrt{(2 \times NIR + 1)^2 - 8 \times (NIR - Red)})}{2}$	Qi et al. (1994)
Normalized Difference Moisture Index	NDMI	$\frac{(NIR - SWIR_1)}{(NIR + SWIR_1)}$	Hardisky et al. (1983)
Normalized Burn Ratio	NBR	$\frac{(NIR - SWIR_2)}{(NIR + SWIR_2)}$	Key and Benson (1999)
Normalized Burn Ratio 2	NBR2	$\frac{(SWIR_1 - SWIR_2)}{(SWIR_1 + SWIR_2)}$	Miller and Thode (2007)
Tasseled Cap Brightness	TCB	$0.3029 \times Blue + 0.2786 \times Green + 0.4733 \times Red + 0.5599 \times NIR + 0.5080 \times SWIR_1 + 0.1872 \times SWIR_2$	Baig et al. (2014)
Tasseled Cap Greenness	TCG	-0.2941 × Blue - 0.2430 × Green - 0.5424 × Red +0.7276 × NIR + 0.0713 × SWIR ₁ - 0.1608 × SWIR ₂	Baig et al. (2014)
Tasseled Cap Wetness	TCW	0.1511 × Blue + 0.1973 × Green + 0.3283 × Red +0.3407 × NIR - 0.7117 × SWIR ₁ - 0.4559 × SWIR ₂	Baig et al. (2014)

sum raster (Fig. 4E). By including these many focal window sizes simultaneously, we allow the subsequent tree crown delineation algorithm to identify both large and small trees alike without having to impose a single window size that might selectively benefit one or the other. This is a key divergence from the approach presented by Rahman

and Gorte (2009), which imposes a single window size.

The remaining steps of the algorithm proceed as follows. The averaged point sum raster was then smoothed using a 3×3 focal filter to remove any remaining imperfections, which can cause additional, erroneous tree crown slivers to be generated. The smoothed raster was

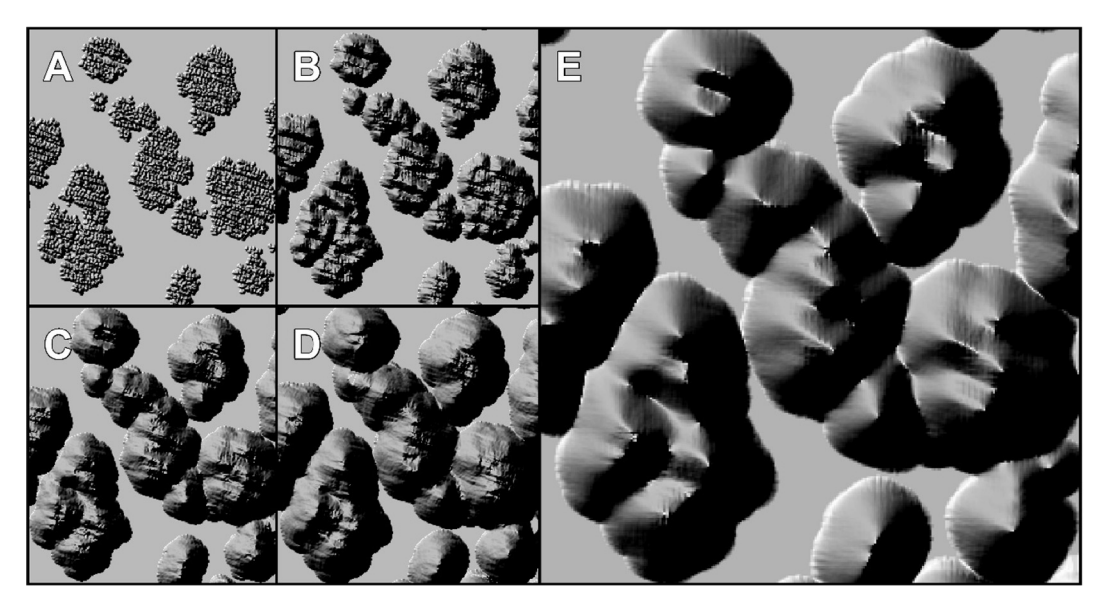


Fig. 4. Comparison of analysis window sizes on focal point sum raster surfaces, including 10 cm (A), 50 cm (B), 100 cm (C), and 150 cm (D), as well as an averaged focal point sum raster surface 10–150 cm (E), all displayed using a hillshade to enhance visual interpretation.

inverted to create a series of focal sum basins rather than focal sum peaks, and then used as input to a watershed delineation algorithm. A canopy height model was then created using the approach presented in Khosravipour et al. (2015). Lastly, all cells above a defined height threshold in the canopy height model were isolated and used to mask out the watersheds, resulting in individual tree crowns. We implemented this tree crown delineation algorithm in Python using Esri ArcGIS geoprocessing tools (Esri, Redlands, California, USA) and applied it to lidar datasets clipped to the extent of our three UAS data collection areas. The resulting polygons were overlaid on top of the UAS imagery in *ArcGIS* and used as a basis of interpreting live vs. dead trees. Each tree polygon was labeled as being either live (< 25% dead vegetation visible within the tree crown polygon), dead (> 75% dead vegetation visible within the tree crown polygon), or partially dead (25-75% dead vegetation visible within the tree crown polygon), according to visual interpretation. Although the focus of this study is on a recent mortality event, it is likely that trees that died prior to 2017 were included in this interpretation. However, retention of needles seen in the field suggests that nearly all of the dead trees within the UAS areas had died in the two years prior to UAS image collection.

3.6. Tree mortality modeling and validation

To scale mortality from the \sim 84 ha of area surveyed by our UAS to Landsat scale, we first created a grid of 30 \times 30 m square polygons aligned to the pixel grid of our Landsat data (Fig. 5). Each pixel in a Landsat 8 L1T-corrected image has an average positional error of approximately \pm 12.6 m (Storey et al., 2014). Due to this spatial registration error – amounting to nearly half of a pixel – it is advisable to avoid using a single pixel as a basis for reference data. Accordingly, we then aggregated those polygons into a series of 90 \times 90 m super-pixels, per the recommendations of Congalton and Green (2008), and randomly split those super-pixels into training (n=25) and validation (n=25). Relative canopy mortality (RCM) was calculated within each super-pixel as follows:

$$RCM = \frac{A_D + 0.5 \times A_{PD}}{A_T},\tag{1}$$

where A_D is total crown area of dead trees, A_{PD} is total crown area of partially dead trees, and A_T is total crown area of all trees (live, dead, and partially dead).

We compared RCM values (dependent variable) to VI difference

values for each of the 11 VI outlined in Table 1 (independent variables) within the training pixels using stepwise linear regression in R (R Core Team, 2018). In order to enhance model parsimony, additional manual independent variable removal was performed on the resulting stepwise regression model. Variables with low significance and high collinearity were removed to create the most robust, and best-fitting multiple regression model. Collinearity among the resulting variables was evaluated by calculating the variance inflation factor for each variable. Model fit was assessed using the coefficient of determination (R²). Given the apparent spatial clustering of mortality, and given the proximal nature of our sampling design, it was possible that spatial autocorrelation between training samples could negatively impact the reliability of our resultant model. To ensure that the assumption of sample independence was met for our modeling procedure, we tested the residual spatial autocorrelation using Moran's I using the lm.morantest() function in the spdep library in R (Bivand et al., 2019).

We then used the 25 validation super-pixels to analyze the performance of the model using R2 and mean absolute error (MAE). Given that a countywide mortality map was generated using training and validation data from a very localized subset of the county, we performed a secondary validation as well using field data collected between 2018 and 2019 throughout SJC. These 15-m radius field plots (n = 35) were strategically-placed within PJ, aimed at capturing a wide range of elevations (1982-2511 m) and RCM (0-58%). RCM values at these plots were compared to mortality map pixel values at plot center and analyzed using R² and MAE. The regression model coefficients were then applied to the VI difference image data in order to create a map of mortality throughout the study area, at a 30 m spatial resolution. Cell values below 0 were coerced to 0 and cell values above 1 were coerced to 1, as it is not possible to have either negative mortality or over 100% mortality for a given pixel. The resulting map was masked to the extent of PJ. In addition, a spatial data set provided by the Bureau of Land Management (BLM) containing the extents of fires and fuel treatments that took place between 2017 and 2019 was used to remove these disturbed sites from the final mortality map. Lastly, descriptive statistics were used to summarize the results.

3.7. Mortality driver analysis

In the interest of uncovering potential drivers of the mortality throughout PJ in SJC, we compared a range of spatial variables to the resulting mortality map. We selected variables in four categories: (1)

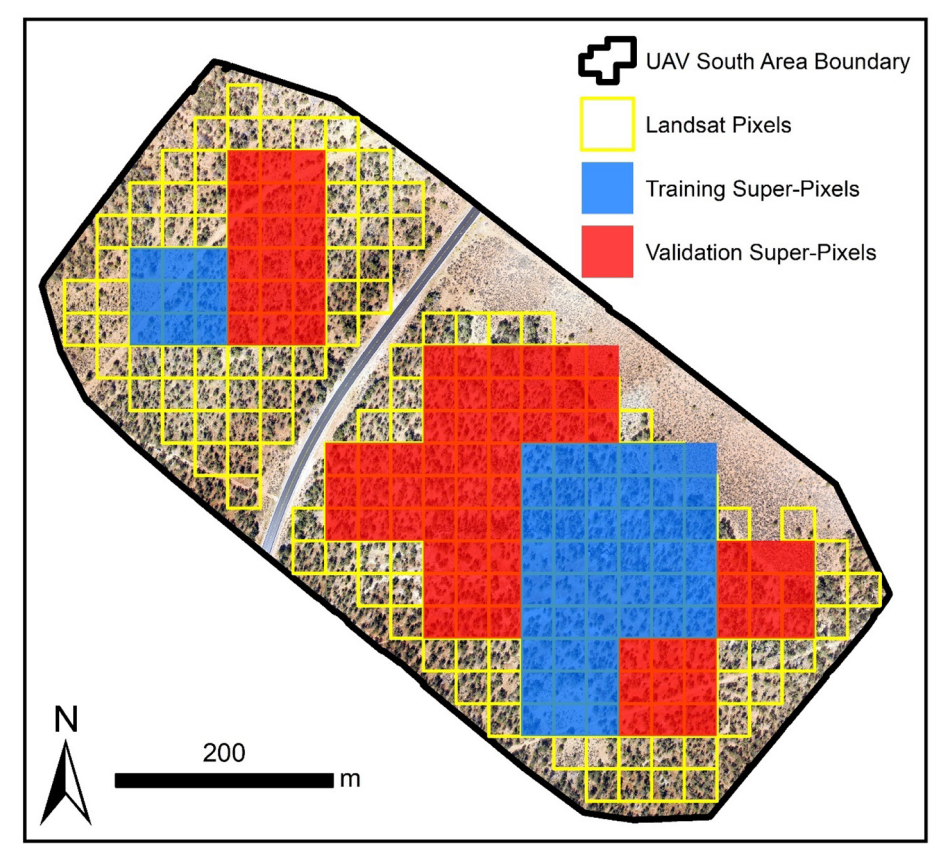


Fig. 5. Map depicting the approach taken to link UAS-lidar canopy mortality estimates to Landsat 8 OLI data.

terrain; (2) climate; (3) soil; and (4) vegetation. For terrain data, 30 m spatial resolution digital elevation models (DEM) were acquired from the USGS 3D Elevation Program (3DEP), and used to generate derivative raster surfaces including slope, cosine of aspect, sine of aspect, curvature, topographic position index (TPI) for a range of radii (10, 20, 30, 40, and 50 cells) (Weiss, 2001), and topographic wetness index (TWI) (Sørensen et al., 2006). For climate data, 4 km spatial resolution monthly temperature (mean, max, and min), precipitation, dew point, and vapor pressure deficit (min and max) data were acquired from PRISM for every month between 1/2017 and 10/2019. In addition. 800 m spatial resolution monthly 30-year normals for all of the same climate variables were also acquired. For soils data, the following rasterized soil parameters from the Gridded National Soil Survey Geographic Database (gNATSGO) (USDA Natural Resources Conservation Service, 2019) were obtained, at each depth range available: available water capacity, available water storage, available water supply, bulk density, calcium carbonate, cation exchange capacity, depth to restrictive layer, depth to water table, drainage class, effective cation exchange capacity, electrical conductivity, gypsum, K factor, linear extensibility, liquid limit, organic matter, percent clay, percent sand, percent silt, pH, plasticity index, saturated hydraulic conductivity, sodium adsorption ratio, surface texture, T factor, water content, and wind erodibility. For vegetation data, the 2016 National Land Cover Database canopy cover dataset was obtained, as was the most recent LANDFIRE fuel vegetation height dataset.

To statistically compare the terrain, climate, soil, and vegetation data to the mortality map, 10,000 random points were created on PJ land in SJC. At each point, mortality map values were extracted along with each of the aforementioned potential mortality driver variables. Point coordinates in the X and Y dimensions were also computed in order to account for potential clustering and spatial autocorrelation in the resulting model. Due to gaps in the gNATSGO data, many sample points were missing soils data. Soil variables that were missing in more

than 20% of points were removed from consideration entirely. Those missing 20% or fewer were approximated using the rfImpute() function in the randomforest library in R, which uses a random forest to estimate unknown values in a dataset (Breiman, 2001; Cutler and Wiener, 2018). The resulting gap-filled data (independent variables) were compared to mortality (dependent variable) using a random forest built with 1000 trees. Variable importance was computed in order to determine which among the many potential drivers had notable effects on mortality. Variables with the highest importance were further examined to determine what specific value ranges were linked to higher mortality by comparing kernel density distributions of high (\geq 10%) mortality pixels vs. low (< 10%) mortality pixels.

4. Results

4.1. Individual tree-level mortality and tree crown delineation results

In all, 18,632 tree crowns were interpreted as live, dead, or partially dead from the UAS imagery (Table 2). By count, the vast majority were found to be alive (84%), but 16% of all trees were dead or partially dead. Even though partially dead trees were smaller in proportion by both count and area than dead trees, the relatively smaller difference in

 Table 2

 Results of individual tree crown mortality interpretation.

Status	Tree count	Tree area (ha)	Proportion by count	Proportion by area
Live	15,692	14.38	84%	83%
Dead	1782	1.51	10%	9%
Partially Dead	1158	1.45	6%	8%
Total	18,632	17.34	100%	100%

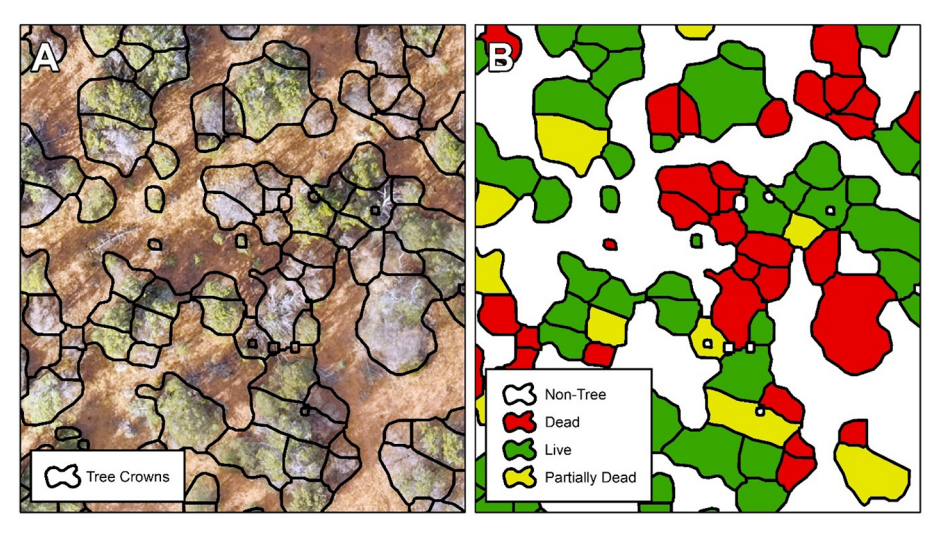


Fig. 6. Map featuring close-up view of tree crown delineation (A) and results of mortality image interpretation (B).

area suggests that partially dead tree crowns tended to be larger than those of dead trees. Although no formal accuracy assessment of our tree crown delineation algorithm was performed, a qualitative, visual assessment reveals that crowns shapes and sizes were accurately represented, though there were certainly examples of under- and oversegmentation (Fig. 6A). Mortality tended to be very localized and patchy in spatial distribution throughout the UAS collection areas (Fig. 6B).

4.2. Stepwise regression model results

The results of the modified stepwise linear regression model for predicting UAS/lidar-derived mortality using Landsat VI difference images can be seen in Table 3. The model resulted in an adjusted $\rm R^2$ of 0.82, suggesting that the combined use of NBR2, TCB, and MSAVI can account for roughly 82% of variance in RCM. Low variance inflation factors among the three predictor variables (NBR2 = 1.77; TCB = 1.43; MSAVI = 1.30) indicates that multicollinearity is low. The results of the test for residual spatial autocorrelation revealed the effects of spatial autocorrelation on our model were negligible. The observed Moran's I value was -0.08 (p = .41), suggesting that any spatial autocorrelation inherent to the model input data was accounted for by the model terms in Table 3. This further suggests that the model diagnostics and parameters are unaffected by spatial autocorrelation and can be viewed as reliable (Gaspard et al., 2019).

The results of the model validation can be seen in Fig. 7. Fig. 7A illustrates the validation results based on the 25 validation super-pixels that were generated using the exact same approach as the training data. According to these results, our model is able to predict RCM with a MAE of 3.43%, meaning that, on average, our model can predict mortality within a margin of error of \pm 3.43% canopy mortality. The regression line comparing predicted mortality to measured mortality has a slope greater than one and a y-intercept greater than zero, suggesting that, on

Table 3 Results of best-fitting, modified stepwise linear regression analysis for predicting relative canopy mortality using Landsat VI difference images. The model has a residual standard error of 3.22% RCM on 21 degrees of freedom (F-statistic = 37.36 on 3 and 21 degrees of freedom, p < .001).

Model Term	Estimate	Standard Error	t-Value	<i>p</i> -Value
NBR2	7.496	0.760	9.859	< 0.001
TCB	4.294	0.532	8.066	< 0.001
MSAVI	-11.740	1.914	-6.133	< 0.001
Intercept	-0.015	0.030		

average, the model will tend to slightly overestimate mortality ($R^2=0.78$). Fig. 7B illustrates the validation results based on the 35 field plots collected throughout the county. Despite the fact that these field plots did not necessarily spatially align with individual Landsat pixels, measured and predicted mortality were still strongly correlated ($R^2=0.71$), although MAE increased to 6.92%. Unlike the image-based validation, the field plot-based validation suggests that, on average, the mortality map will likely underestimate true mortality, particularly at higher-mortality sites.

It was impossible to determine the species of the dead trees using the UAS data alone. However, while collecting the UAS data, we qualitatively observed that the majority of mortality within the UAS sample areas was among piñon pines. The field plot validation data, however, provided robust, quantitative insight into the relative species distribution of mortality. Across all 35 plots, the mortality was roughly evenly distributed between piñon (9.9% average mortality) and juniper (10.0% average mortality), with 18 of the plots featuring higher piñon mortality and 17 featuring higher juniper mortality. There was no readily observable spatial patterning of piñon vs. juniper mortality among the plot locations. The relative abundance of juniper mortality stands in contrast to recent historic PJ mortality events, where the mortality was found primarily in piñon pines (Shaw et al., 2005).

4.3. Regional tree mortality results

The resulting mortality map based on the stepwise regression model can be seen in Fig. 8. While most of the PJ throughout the study area appears to have low mortality (as indicated by the blue colour), higher mortality patches are evident. For example, in Fig. 8C, D, and E, three distinct patches of mortality are displayed in higher detail, where some pixels are modeled with mortality greater than 50%. Quantitative mortality area and proportional summaries can be seen in Fig. 9. According to these results, nearly 39% of all PJ in SJC has experienced at least 5% RCM, and over a quarter has experienced at least 10% RCM. Very high mortality areas (> 50%) are very rare, representing less than 1% of all PJ in SJC.

4.4. Mortality driver results

The random forest model aimed at linking terrain, climate, soil, and vegetation spatial variables to mortality resulted in relatively low explanatory power, with only 16.8% of variance in mortality explained by the large number of predictors (mean of squared residuals = 0.01). Despite the low explanatory power, it is still informative to look at which predictor variables had a comparably significant relationship

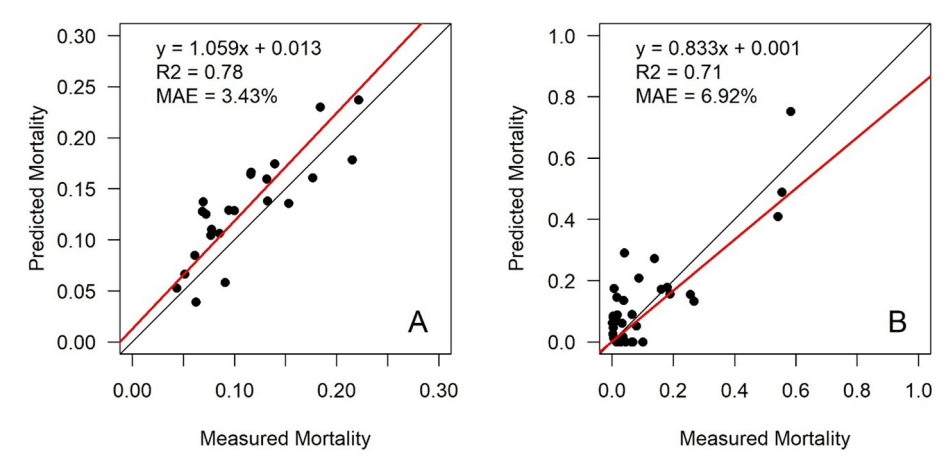


Fig. 7. Validation results of the mortality predictive model using the 25 validation super-pixels (A) and the 35 field validation plots (B). The 1:1 line is shown in black. The regression line is shown in red. (For interpretation of the references to colour in this figure legend, the reader is referred to the web version of this article.)

with mortality. Random forests allow for the calculation of variable importance through the calculation of the relative increase in predictive mean squared error that results when a given variable is removed from consideration (Fig. 10). By this measure, four particular variables appeared to have the most significant influence on mortality: canopy cover, precipitation for January 2019, topographic position index at a radius of 50 raster cells, and slope. Following the top four there is a notable decrease in variable importance, with terrain variables

generally having the highest influence among the remaining variables, including topographic position indices and curvature. Notably, neither aspect nor topographic wetness index had a significant effect on mortality. Also of note is the relatively low influence of elevation, though this may be attributable to the fact that the climate datasets tested are highly correlated with elevation. Over half of the top 30 most important variables belong to the climate category, with winter precipitation totals and vapor pressure deficits playing a dominant role in the

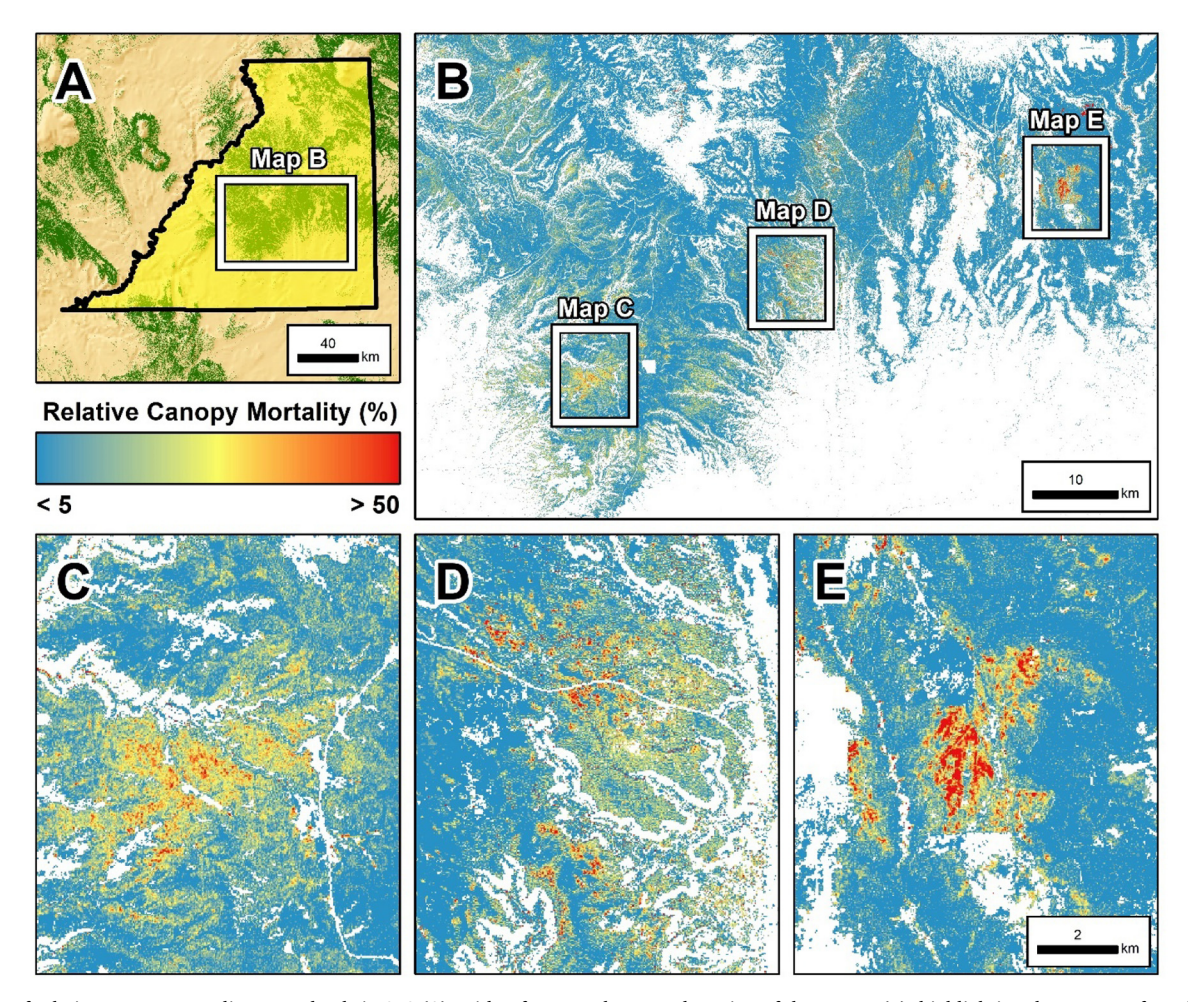


Fig. 8. Map of relative canopy mortality on PJ lands in SJC (A), with a focus on the central portion of the county (B), highlighting three areas of particularly high mortality (C, D, and E).

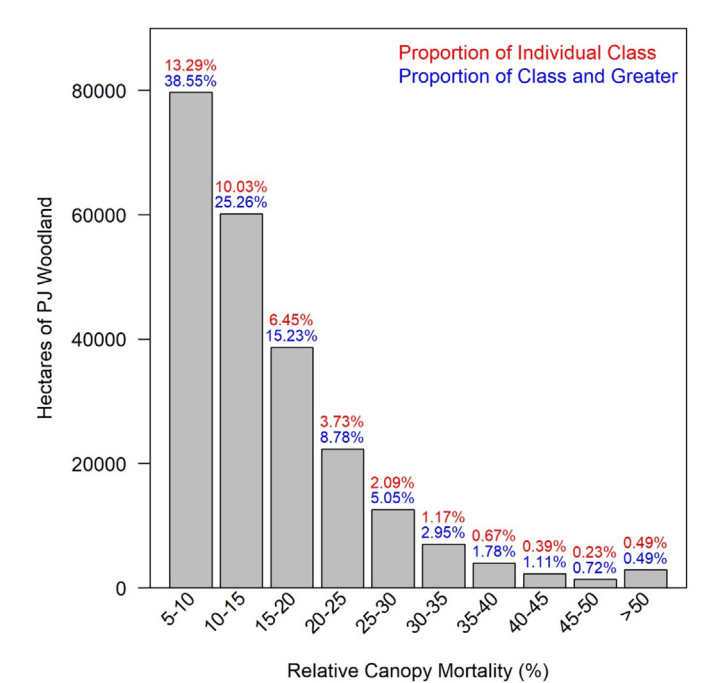


Fig. 9. Histogram of PJ mortality totals by 5% mortality intervals, with area in hectares, proportion of individual classes in red, and proportion of each class and greater in blue. (For interpretation of the references to colour in this figure legend, the reader is referred to the web version of this article.)

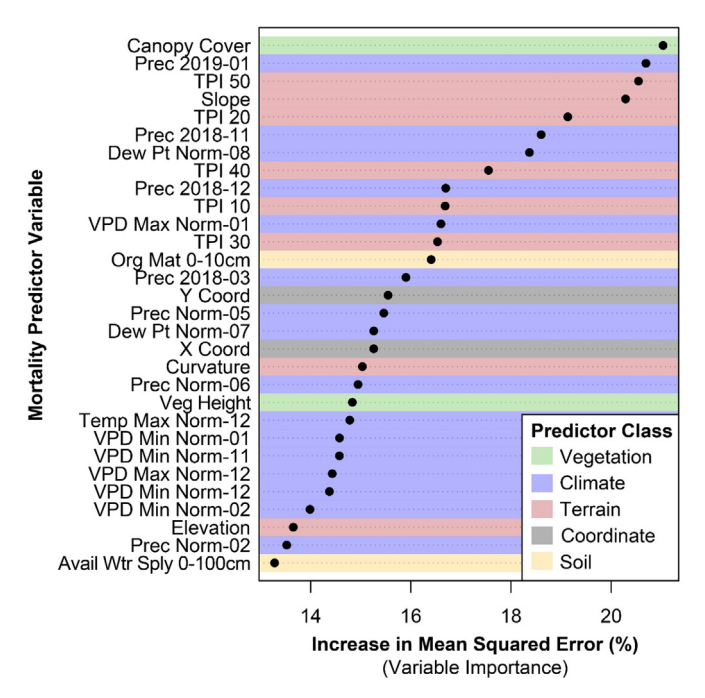


Fig. 10. Variable importance as measured by increase in mean squared error of the top 30 climate, terrain, vegetation, and soil variables used in a random forest model aimed at estimating tree mortality. Variable definitions can be found in Table S2.

prediction of mortality. Soil variables were generally found to have lower importance than climate, terrain, and vegetation, with only two soil variables (organic matter 0–10 cm and available water supply 0–100 cm) in the top 30. Lastly, due to the clustered nature of the mortality, both the X and Y coordinates of the sample points were included in the most important variable list, suggesting some level of spatial autocorrelation in the dataset.

Fig. 11 provides insight into the ranges of values among the top four most important predictors where you are more likely to find high (≥ 10%) mortality sites vs. low (< 10%) mortality sites based on a comparison of kernel density distributions. For example, high mortality sites are more likely to be found in areas with low-moderate canopy cover (5–25%), which contrasts with a prevailing view that high canopy cover sites are more prone to mortality due to resource competition or higher likelihood of pest invasion (Meddens et al., 2015). In addition, higher mortality sites tend to be found within areas that featured relatively lower precipitation in January 2019. Given that the majority of winter precipitation in this region comes in the form of snow, this would suggest that a lower winter snowfall in this month may be linked to mortality. Mortality tends to be higher where the TPI 50 is less than zero. Since TPI is a measure of relative elevation in comparison to surrounding elevations at a given radius (in this case, 50×30 m cells = 1500 m), this can be interpreted as suggesting that high mortality sites tend to be found in regional low points. Lastly, areas featuring lower terrain slopes (< 10°) are more likely to feature high mortality than steeper areas.

5. Discussion

Our use of centimeter-scale UAS imagery and lidar was necessary to overcome the challenges of mapping mortality in a sparse, open canopy woodland in a semiarid environment. UAS are capable of producing sufficiently high resolution for the interpretation of live vs. dead trees and distinction between ground, understory, and canopy. In addition to being higher resolution than most traditional airborne surveys, UAS data can be collected on-demand at a very low cost, which can be greatly beneficial when attempting to map an acute and on-going mortality event, as compared to traditional airborne surveys, which capture data relatively infrequently. Lidar data provided crown delineation, but did not need to be concurrent with UAS data. In environments featuring trees with more regular (e.g. conical or rounded) crown shapes, the application of a structure from motion algorithm directly on UAS imagery could potentially replace the need for lidar altogether (Sankey et al., 2017); however, in PJ woodland our lidar point densitybased crown delineation algorithm proved necessary for accurate treelevel mortality quantification.

The results of previous multi-scale, multi-sensor mortality mapping efforts took the form of a classified map, with mortality map pixels belonging to one of several discrete categories (e.g. "live", "red stage mortality", or "gray stage mortality") (Hart and Veblen, 2015; He et al., 2019; Meddens et al., 2013). While this is certainly useful information for mapping the extent of mortality, it does not provide a within-stand (or, within-pixel) measure of quantitative mortality. Identification of tree-level mortality through the use of combined UAS and lidar data allowed scaling of percent mortality (as measured by RCM), which should be a more useful parameter for use with spatial models such as ecosystem demography models (Bugmann et al., 2019; Hartmann et al., 2018; Meir et al., 2015). The additional precision in our mortality map will also facilitate a more informed follow-up field campaign, allowing a closer, ground-level examination of the factors that might be driving high vs. low mortality.

It is important to carefully examine the results of the regression analysis that allowed us to upscale the UAS/lidar-derived mortality estimates to the Landsat level. Unlike some more complex methodologies, regression analysis benefits from its simplicity, and its ability to directly assess the magnitude and direction of individual model coefficients, which can reveal important physical processes. As Table 3 highlights, the coefficients for NBR2 and TCB are positive, suggesting that with increasing canopy mortality comes an increase in NBR2 and TCB. NBR2 is a normalized difference between SWIR1 and SWIR2 bands (Table 1). A closer examination of our data reveals that, while SWIR1 reflectance increased from 2017 to 2019, SWIR2 saw little change in this time frame. We attribute the stability in SWIR2 reflectance to the

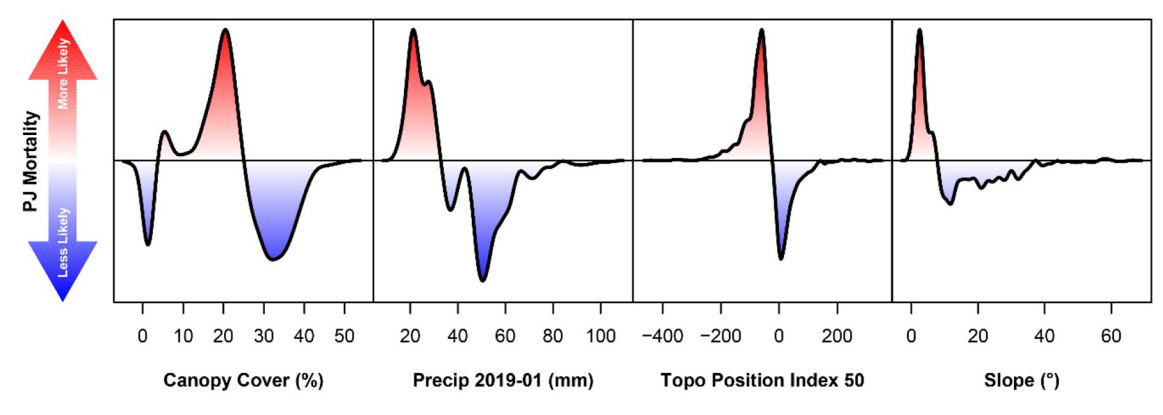


Fig. 11. Comparison of mortality predictor variable distribution between high ($\geq 10\%$) and low (< 10%) mortality areas. Areas above the horizonal line for each plot indicate that high mortality sites are more likely to be found than low mortality sites. Areas below the horizontal line indicate the opposite.

abundance of dead, dry needles, wood, and other non-photosynthetic vegetation present in the post-mortality pixels causing lignocellulose absorption in the $SWIR_2$ region (2.10–2.30 μm), offsetting the effects of decreasing live foliage (Souza et al., 2005). Thus, an NBR2 increase between these time frames is attributed to a shift from photosynthetic vegetation to non-photosynthetic vegetation cover due to tree mortality. TCB is aimed at approximating the overall brightness (total reflectance) of the constituent materials found within a pixel. Thus, a decrease in vegetation cover results in an increase in reflectance, due to increased exposure of less absorptive materials such as non-photosynthetic vegetation, soil, and rock. Conversely, MSAVI has a negative coefficient, suggesting that with increasing canopy mortality comes a decrease in MSAVI. These results align with the conceptual basis of MSAVI, which aims to quantify vegetation biomass in arid environments such as our study area.

We are using three small areas of UAS imagery (totaling 83.6 ha), collected only in one portion of the study area, as a reference dataset driving a regression analysis that is aimed at mapping conditions over a diversity of all PJ in a large study area. While such an experimental design could lend itself to problems associated with extrapolation, an extensive field campaign resulting in 35 plots that capture mortality conditions across ecological gradients throughout the broader study area demonstrated that our model's predictive power and map accuracy are still quite high (Fig. 7B).

Although the focus of this study is on PJ woodlands, the methods described for mapping and quantifying tree mortality herein may be applicable in a diverse range of semiarid woodland ecosystems. These sparsely-canopied environments are particularly susceptible to increasingly severe and extended droughts that are anticipated with changes to the climate (Breshears et al., 2016). Given the extent of woodland ecosystems worldwide, and with semiarid and other dryland biomes expected to expand by as much as 23% by the end of the 21st century, we anticipate that the methodology we have introduced could have very broad and increasingly useful applicability in the future (Huang et al., 2016).

The patchy and clustered nature of the mortality suggests that there are perhaps some common drivers of mortality that are present in highmortality patches and absent in low/no-mortality patches. We used modern machine learning tools and a whole suite of variables to attempt to explain the spatial distribution of the mortality, but the explanatory power was relatively low. This may be a result of one or both of two things: (1) some other driver(s) that we did not test was/were responsible for explaining the other 83.2% of mortality; or (2) the drivers we analyzed were largely responsible, but the spatial datasets that represent them are simply insufficient for characterizing mortality at such a local scale. For instance, even under experimentally-controlled drought conditions, PJ trees can survive due to conditions like access to bedrock water, which could not be accounted for given the

coarseness of the soils data used in our study (McDowell et al., 2019). At this point, it is impossible to know which of the two is more likely, but due to past evidence linking drought to mortality and due to the lack of any evidence in the field of pests or pathogens as mortality drivers, we suspect that the second case is more likely.

It is important to note that terrain and vegetation variables – the variables that had the highest importance in predicting mortality – were also from the highest-resolution data sources. Thus, their importance may be simply a result of their increased capacity for capturing the local-scale variation in mortality as compared to the 4 km resolution climate data and the soils data. A comprehensive review of piñon mortality by Meddens et al. (2015) suggests that all four driver categories tested in our study (terrain, climate, soil, and vegetation), as well as some additional factors, such as individual tree-levels metrics (e.g. tree size) and presence of pests, likely interact in variable and complex ways to cause mortality. Although our study area was limited to the extent of SJC, the diverse range of environmental and climatic conditions captured in this very large county – larger than several, individual US states in area – provides valuable insight into broader regional drivers of tree mortality.

6. Conclusions

In this study we present a novel approach to mapping the extent and severity of tree mortality in a sparse, open canopy woodland using UAS to map individual tree-level mortality and distinguish canopy from understory within small areas, airborne lidar to delineate individual tree crowns to enable accurate canopy cover and relative mortality proportion calculations, and Landsat 8 OLI imagery to scale up local estimates of mortality to a broad spatial scale. Although we are not the first to utilize a multi-scale, multi-sensor approach to mapping tree mortality, we have built upon previous research to develop an approach that is better-suited to the complexities of woodland environments. Given the widespread distribution of PJ and other structurally-similar woodland types globally, and the critical roles that they play ecologically, it is of crucial importance to develop customized, yet broadly-applicable, mapping solutions for these ecosystems, as we have presented here.

Between 2017 and 2019, 39% of PJ land in SJC has experienced ≥5% RCM, and over one quarter has experienced at least 10% RCM. Importantly, due to the timing of this analysis, it remains unclear whether this mortality event is going to continue into the future. But even in the absence of continued tree die-off, the mortality totals we have documented are quite significant. In an ecosystem as widespread as PJ that provides a range of important ecosystem services, the loss of these woodland trees can have a dramatic impact on much of the southwestern US. Particularly when looking back to the major PJ mortality event that occurred in the early 2000s, it becomes

particularly concerning to think that this recent mortality event may not be an outlier, but perhaps one in a sequence of continued climate-driven mortality events that will continue into the future (Williams et al., 2013).

Although our study did not definitively explain the causes of this mortality event, recent historical evidence suggests that drought, as manifested by a unique combination of climate, terrain, vegetation, and soil parameters, is driving the die-off. Among these parameters, we were able to determine that regional low points featuring low-moderate canopy covers and low slopes that had a relatively dry January 2019 were most likely to feature high mortality sites within our study area, although this model had low explanatory power. Future field data collection measuring variables within the high-mortality areas mapped in this study could be used to inquire into mortality drivers with a finer precision than can be afforded using coarse spatial datasets alone.

Funding

This research was funded by the National Science Foundation, grant number DEB-1714972.

SAK is supported by the NSF Ecosystem Science cluster, grant #1753845. Funding for some of the field work was provided by the USDA Forest Service Evaluation Monitoring program.

Acknowledgments

Thanks to Avery Driscoll, Paul Kuenker, and Jared Beeton for their support in collecting field data, and to Jonathan Jew for providing BLM fuel treatment and fire spatial data.

Declaration of Competing Interest

The authors declare that they have no known competing financial interests or personal relationships that could have appeared to influence the work reported in this paper.

Appendix A. Supplementary data

Supplementary data to this article can be found online at https://doi.org/10.1016/j.rse.2020.111853.

References

- Ahlström, A., Raupach, M.R., Schurgers, G., Smith, B., Arneth, A., Jung, M., Reichstein, M., Canadell, J.G., Friedlingstein, P., Jain, A.K., Kato, E., Poulter, B., Sitch, S., Stocker, B.D., Viovy, N., Wang, Y.P., Wiltshire, A., Zaehle, S., Zeng, N., 2015. The dominant role of semi-arid ecosystems in the trend and variability of the land CO2 sink. Science 348, 895–899. https://doi.org/10.1126/science.aaa1668.
- Allen, C.D., Breshears, D.D., McDowell, N.G., 2015. On underestimation of global vulnerability to tree mortality and forest die-off from hotter drought in the Anthropocene. Ecosphere 6. https://doi.org/10.1890/ES15-00203.1. art129.
- Anderegg, W.R.L., Kane, J.M., Anderegg, L.D.L., 2013. Consequences of widespread tree mortality triggered by drought and temperature stress. Nat. Clim. Chang. 3, 30–36. https://doi.org/10.1038/nclimate1635.
- Anderegg, W.R.L., Hicke, J.A., Fisher, R.A., Allen, C.D., Aukema, J., Bentz, B., Hood, S., Lichstein, J.W., Macalady, A.K., McDowell, N., Pan, Y., Raffa, K., Sala, A., Shaw, J.D., Stephenson, N.L., Tague, C., Zeppel, M., 2016. Tree mortality from drought, insects, and their interactions in a changing climate. New Phytol. 674-683. https://doi.org/10.1111/ph.13477@10.1111/(ISSN)1469-8137.Highlightsof2015.
- Badgley, G., Field, C.B., Berry, J.A., 2017. Canopy near-infrared reflectance and terrestrial photosynthesis. Sci. Adv. 3, e1602244. https://doi.org/10.1126/sciadv.1602244.
- Baig, M.H.A., Zhang, L., Shuai, T., Tong, Q., 2014. Derivation of a tasselled cap transformation based on Landsat 8 at-satellite reflectance. Remote Sensing Lett. 5, 423–431. https://doi.org/10.1080/2150704X.2014.915434.
- Bastin, J.-F., Berrahmouni, N., Grainger, A., Maniatis, D., Mollicone, D., Moore, R., Patriarca, C., Picard, N., Sparrow, B., Abraham, E.M., Aloui, K., Atesoglu, A., Attore, F., Bassüllü, Ç., Bey, A., Garzuglia, M., García-Montero, L.G., Groot, N., Guerin, G., Laestadius, L., Lowe, A.J., Mamane, B., Marchi, G., Patterson, P., Rezende, M., Ricci, S., Salcedo, I., Diaz, A.S.-P., Stolle, F., Surappaeva, V., Castro, R., 2017. The extent of forest in dryland biomes. Science 356, 635–638. https://doi.org/10.1126/science.aam6527.
- Bivand, R., Altman, M., Anselin, L., Assunção, R., Berke, O., Bernat, A., Blanchet, G.,

- Blankmeyer, E., Carvalho, M., Christensen, B., Chun, Y., Dormann, C., Dray, S., Gómez-Rubio, V., Gubri, M., Halbersma, R., Krainski, E., Legendre, P., Lewin-Koh, N., Li, A., Li, H., Ma, J., Mallik, A., Millo, G., Mueller, W., Ono, H., Peres-Neto, P., Piras, G., Reder, M., Tiefelsdorf, M., Westerholt, R., Yu, D., 2019. spdep: Spatial Dependence: Weighting Schemes, Statistics.
- Breiman, L., 2001. Random forests. Mach. Learn. 45, 5–32. https://doi.org/10.1023/
- Breshears, D.D., Cobb, N.S., Rich, P.M., Price, K.P., Allen, C.D., Balice, R.G., Romme, W.H., Kastens, J.H., Floyd, M.L., Belnap, J., Anderson, J.J., Myers, O.B., Meyer, C.W., 2005. Regional vegetation die-off in response to global-change-type drought. PNAS 102, 15144–15148. https://doi.org/10.1073/pnas.0505734102.
- Breshears, D.D., Knapp, A.K., Law, D.J., Smith, M.D., Twidwell, D., Wonkka, C.L., 2016. Rangeland responses to predicted increases in drought extremity. Rangelands, Drought on Rangelands: Effects and Solutions 38, 191–196. https://doi.org/10.1016/i.rala.2016.06.009.
- Bugmann, H., Seidl, R., Hartig, F., Bohn, F., Brûna, J., Cailleret, M., François, L., Heinke, J., Henrot, A.-J., Hickler, T., Hülsmann, L., Huth, A., Jacquemin, I., Kollas, C., Lasch-Born, P., Lexer, M.J., Merganič, J., Merganičová, K., Mette, T., Miranda, B.R., Nadal-Sala, D., Rammer, W., Rammig, A., Reineking, B., Roedig, E., Sabaté, S., Steinkamp, J., Suckow, F., Vacchiano, G., Wild, J., Xu, C., Reyer, C.P.O., 2019. Tree mortality submodels drive simulated long-term forest dynamics: assessing 15 models from the stand to global scale. Ecosphere 10, e02616. https://doi.org/10.1002/ecs2.2616.
- Bullock, E.L., Woodcock, C.E., Olofsson, P., 2020. Monitoring tropical forest degradation using spectral unmixing and Landsat time series analysis. Remote Sensing of Environment, Time Series Analysis with High Spatial Resolution Imagery 238, 110968. https://doi.org/10.1016/j.rse.2018.11.011.
- Clark, D.B., Castro, C.S., Alvarado, L.D.A., Read, J.M., 2004. Quantifying mortality of tropical rain forest trees using high-spatial-resolution satellite data. Ecol. Lett. 7, 52–59. https://doi.org/10.1046/j.1461-0248.2003.00547.x.
- Clifford, M.J., Cobb, N.S., Buenemann, M., 2011. Long-term tree cover dynamics in a pinyon-Juniper woodland: climate-change-type drought resets successional clock. Ecosystems 14, 949–962. https://doi.org/10.1007/s10021-011-9458-2.
- Clifford, M.J., Royer, P.D., Cobb, N.S., Breshears, D.D., Ford, P.L., 2013. Precipitation thresholds and drought-induced tree die-off: insights from patterns of Pinus edulis mortality along an environmental stress gradient. New Phytol. 200, 413–421. https://doi.org/10.1111/nph.12362.
- Coates, P.S., Prochazka, B.G., Ricca, M.A., Gustafson, K.B., Ziegler, P., Casazza, M.L., 2017. Pinyon and Juniper encroachment into sagebrush ecosystems impacts distribution and survival of greater sage-grouse. Rangeland Ecology & Management, Woody invasion of western rangelands: Using grouse as focal species for ecosystem restoration 70, 25–38. https://doi.org/10.1016/j.rama.2016.09.001.
- Congalton, R.G., Green, K., 2008. Assessing the Accuracy of Remotely Sensed Data: Principles and Practices. CRC Press, Second Edition.
- Coops, N.C., Waring, R.H., Wulder, M.A., White, J.C., 2009. Prediction and assessment of bark beetle-induced mortality of lodgepole pine using estimates of stand vigor derived from remotely sensed data. Remote Sens. Environ. 113, 1058–1066. https:// doi.org/10.1016/j.rse.2009.01.013.
- Core Team, R., 2018. R: A Language and Environment for Statistical Computing. R Foundation for Statistical Computing, Vienna, Austria.
- Cutler, F., original by L.B. and A., Wiener, R. port by A.L. and M, 2018. randomForest: Breiman and Cutler's Random Forests for Classification and Regression.
- Filippelli, S.K., Falkowski, M.J., Hudak, A.T., Fekety, P., Vogeler, J.C., Khalyani, A.H., Rau, B.M., Strand, E.K., 2020. Monitoring pinyon-juniper cover and aboveground biomass across the Great Basin. Environ. Res. Lett. https://doi.org/10.1088/1748-9326/ab6785.
- Fortin, J.A., Cardille, J.A., Perez, E., 2020. Multi-sensor detection of forest-cover change across 45 years in Mato Grosso, Brazil. Remote Sensing of Environment, Time Series Analysis with High Spatial Resolution Imagery 238, 111266. https://doi.org/10. 1016/i.rse.2019.111266.
- Fraser, R.H., Latifovic, R., 2005. Mapping insect-induced tree defoliation and mortality using coarse spatial resolution satellite imagery. Int. J. Remote Sens. 26, 193–200. https://doi.org/10.1080/01431160410001716923.
- Garrity, S.R., Allen, C.D., Brumby, S.P., Gangodagamage, C., McDowell, N.G., Cai, D.M., 2013. Quantifying tree mortality in a mixed species woodland using multitemporal high spatial resolution satellite imagery. Remote Sens. Environ. 129, 54–65. https:// doi.org/10.1016/j.rse.2012.10.029.
- Gaspard, G., Kim, D., Chun, Y., 2019. Residual spatial autocorrelation in macroecological and biogeographical modeling: a review. J Ecol. Environ. 43, 19. https://doi.org/10. 1186/s41610-019-0118-3.
- Gori, D., Bate, J., 2007. Historical range of variation and state and transition modeling of historical and current landscape conditions for pinyon-juniper of the southwestern US. In: Tucson, A.Z. (Ed.), USA: Prepared for the US Forest Service, Southwestern Region by The Nature Conservancy, 141p.
- Greenwood, D.L., Weisberg, P.J., 2008. Density-dependent tree mortality in pinyon-juniper woodlands. Forest Ecology and Management, Large-scale experimentation and oak regeneration 255, 2129–2137. https://doi.org/10.1016/j.foreco.2007.12.048.
- Guo, Q., Kelly, M., Gong, P., Liu, D., 2007. An object-based classification approach in mapping tree mortality using high spatial resolution imagery. GIScience & Remote Sensing 44, 24–47. https://doi.org/10.2747/1548-1603.44.1.24.
- Hardisky, M., Klemas, V., Smart, R., 1983. Close the influence of soil salinity, growth form and leaf moisture on the spectral radiance of Spartina alterniflora canopies. Photogramm. Eng. Remote. Sens. 49, 77–83.
- Hart, S.J., Veblen, T.T., 2015. Detection of spruce beetle-induced tree mortality using high- and medium-resolution remotely sensed imagery. Remote Sens. Environ. 168, 134–145. https://doi.org/10.1016/j.rse.2015.06.015.
- Hartmann, H., Moura, C.F., Anderegg, W.R.L., Ruehr, N.K., Salmon, Y., Allen, C.D., Arndt,

- S.K., Breshears, D.D., Davi, H., Galbraith, D., Ruthrof, K.X., Wunder, J., Adams, H.D., Bloemen, J., Cailleret, M., Cobb, R., Gessler, A., Grams, T.E.E., Jansen, S., Kautz, M., Lloret, F., O'Brien, M., 2018. Research frontiers for improving our understanding of drought-induced tree and forest mortality. New Phytol. 218, 15–28. https://doi.org/10.1111/nph.15048.
- He, Y., Chen, G., Potter, C., Meentemeyer, R.K., 2019. Integrating multi-sensor remote sensing and species distribution modeling to map the spread of emerging forest disease and tree mortality. Remote Sens. Environ. 231, 111238. https://doi.org/10. 1016/j.rse.2019.111238.
- Huang, C., Asner, G.P., Martin, R.E., Barger, N.N., Neff, J.C., 2009. Multiscale analysis of tree cover and aboveground carbon stocks in pinyon–juniper woodlands. Ecol. Appl. 19, 668–681. https://doi.org/10.1890/07-2103.1.
- Huang, J., Yu, H., Guan, X., Wang, G., Guo, R., 2016. Accelerated dryland expansion under climate change. Nat. Clim. Chang. 6, 166–171. https://doi.org/10.1038/ nclimate/2837
- Huete, A.R., 1988. A soil-adjusted vegetation index (SAVI). Remote Sens. Environ. 25, 295–309. https://doi.org/10.1016/0034-4257(88)90106-X.
- Key, C.H., Benson, N.C., 1999. The Normalized Burn Ratio (NBR): A Landsat TM Radiometric Measure of Burn Severity. United States Geological Survey, Northern Rocky Mountain Science Center. Bozeman, MT.
- Khosravipour, A., Skidmore, A.K., Wang, T., Isenburg, M., Khoshelham, K., 2015. Effect of slope on treetop detection using a LiDAR canopy height model. ISPRS J. Photogramm. Remote Sens. 104, 44–52. https://doi.org/10.1016/j.isprsjprs.2015. 02.013.
- Krofcheck, D.J., Litvak, M.E., Lippitt, C.D., Neuenschwander, A., 2016. Woody biomass estimation in a southwestern U.S. Juniper savanna using LiDAR-derived clumped tree segmentation and existing Allometries. Remote Sens. 8, 453. https://doi.org/10. 3390/rs8060453.
- Linton, M.J., Sperry, J.S., Williams, D.G., 1998. Limits to water transport in Juniperus osteosperma and Pinus edulis: implications for drought tolerance and regulation of transpiration. Funct. Ecol. 12, 906–911. https://doi.org/10.1046/j.1365-2435.1998.
- Liu, H.Q., Huete, A., 1995. A feedback based modification of the NDVI to minimize canopy background and atmospheric noise. IEEE Trans. Geosci. Remote Sens. 33, 457–465. https://doi.org/10.1109/TGRS.1995.8746027.
- Macomber, S.A., Woodcock, C.E., 1994. Mapping and monitoring conifer mortality using remote sensing in the Lake Tahoe Basin. Remote Sens. Environ. 50, 255–266. https:// doi.org/10.1016/0034-4257(94)90075-2.
- Matusick, G., Ruthrof, K.X., Hardy, G.E.S.J., 2012. Drought and heat triggers sudden and severe dieback in a dominant Mediterranean-type woodland species. Open Journal of Forestry 02. 183–186.
- McDowell, N.G., Grossiord, C., Adams, H.D., Pinzón-Navarro, S., Mackay, D.S., Breshears, D.D., Allen, C.D., Borrego, I., Dickman, L.T., Collins, A., Gaylord, M., McBranch, N., Pockman, W.T., Vilagrosa, A., Aukema, B., Goodsman, D., Xu, C., 2019. Mechanisms of a coniferous woodland persistence under drought and heat. Environ. Res. Lett. 14, 045014. https://doi.org/10.1088/1748-9326/ab0921.
- Meddens, A.J.H., Hicke, J.A., 2014. Spatial and temporal patterns of Landsat-based detection of tree mortality caused by a mountain pine beetle outbreak in Colorado, USA. For. Ecol. Manag. 322, 78–88. https://doi.org/10.1016/j.foreco.2014.02.037.
- Meddens, A.J.H., Hicke, J.A., Vierling, L.A., Hudak, A.T., 2013. Evaluating methods to detect bark beetle-caused tree mortality using single-date and multi-date Landsat imagery. Remote Sens. Environ. 132, 49–58. https://doi.org/10.1016/j.rse.2013.01. 002.
- Meddens, A.J.H., Hicke, J.A., Macalady, A.K., Buotte, P.C., Cowles, T.R., Allen, C.D., 2015. Patterns and causes of observed piñon pine mortality in the southwestern United States. New Phytol. 206, 91–97. https://doi.org/10.1111/nph.13193.
- Meigs, G.W., Kennedy, R.E., Cohen, W.B., 2011. A Landsat time series approach to characterize bark beetle and defoliator impacts on tree mortality and surface fuels in conifer forests. Remote Sens. Environ. 115, 3707–3718. https://doi.org/10.1016/j. rse.2011.09.009.
- Meir, P., Mencuccini, M., Dewar, R.C., 2015. Drought-related tree mortality: addressing the gaps in understanding and prediction. New Phytol. 207, 28–33. https://doi.org/ 10.1111/nph.13382.
- Miller, J.D., Thode, A.E., 2007. Quantifying burn severity in a heterogeneous landscape with a relative version of the delta normalized burn ratio (dNBR). Remote Sens. Environ. 109, 66–80. https://doi.org/10.1016/j.rse.2006.12.006.
- Miller, R.F., Rose, J.A., 1999. Fire history and western juniper encroachment in sagebrush steppe. J. Range Manag. 52, 550–559.

- 001481
- Qi, J., Chehbouni, A., Huete, A.R., Kerr, Y.H., Sorooshian, S., 1994. A modified soil adjusted vegetation index. Remote Sens. Environ. 48, 119–126. https://doi.org/10.1016/0034-4257(94)90134-1.
- Rahman, M.Z.A., Gorte, B.G.H., 2009. Tree crown delineation from high resolution airborne LiDAR based on densities of high points. In: Proceedings ISPRS Workshop Laserscanning 2009, September 1–2, France, IAPRS, XXXVIII (3/W8). ISPRS.
- Ratnam, J., Bond, W.J., Fensham, R.J., Hoffmann, W.A., Archibald, S., Lehmann, C.E.R., Anderson, M.T., Higgins, S.I., Sankaran, M., 2011. When is a 'forest' a savanna, and why does it matter? Glob. Ecol. Biogeogr. 20, 653–660. https://doi.org/10.1111/j. 1466-8238.2010.00634.x.
- Rollins, M.G., 2009. LANDFIRE: a nationally consistent vegetation, wildland fire, and fuel assessment. Int. J. Wildland Fire 18, 235–249. https://doi.org/10.1071/WF08088. Rouse, J.W., 1974. Monitoring Vegetation Systems in the Great Plains with ERTS.
- Samuels, M.L., Betancourt, J.L., 1982. Modeling the long-term effects of fuelwood harvests on pinyon-Juniper woodlands. Environ. Manag. 6, 505–515. https://doi.org/10.
- Sankey, T., Donager, J., McVay, J., Sankey, J.B., 2017. UAV lidar and hyperspectral fusion for forest monitoring in the southwestern USA. Remote Sens. Environ. 195, 30–43. https://doi.org/10.1016/j.rse.2017.04.007.
- Shaw, J.D., Steed, B.E., DeBlander, L.T., 2005. Forest Inventory and Analysis (FIA) Annual Inventory Answers the Question: What Is Happening to Pinyon-Juniper Woodlands? J for 103. pp. 280–285. https://doi.org/10.1093/jof/103.6.280.
- Short, H.L., McCulloch, C.Y., 1977. Managing pinyon-juniper ranges for wildlife. In: Rocky Mountain Forest and Range Experiment Station, Forest Service, US.
- Smith, W.K., Dannenberg, M.P., Yan, D., Herrmann, S., Barnes, M.L., Barron-Gafford, G.A., Biederman, J.A., Ferrenberg, S., Fox, A.M., Hudson, A., Knowles, J.F., MacBean, N., Moore, D.J.P., Nagler, P.L., Reed, S.C., Rutherford, W.A., Scott, R.L., Wang, X., Yang, J., 2019. Remote sensing of dryland ecosystem structure and function: Progress, challenges, and opportunities. Remote Sens. Environ. 233, 111401. https://doi.org/10.1016/j.rse.2019.111401.
- Sørensen, R., Zinko, U., Seibert, J., 2006. On the calculation of the topographic wetness index: evaluation of different methods based on field observations. Hydrol. Earth Syst. Sci. Discuss. 10, 101–112.
- Souza, C.M., Roberts, D.A., Cochrane, M.A., 2005. Combining spectral and spatial information to map canopy damage from selective logging and forest fires. Remote Sens. Environ. 98, 329–343. https://doi.org/10.1016/j.rse.2005.07.013.
- Storey, J., Choate, M., Lee, K., 2014. Landsat 8 operational land imager on-orbit geometric calibration and performance. Remote Sens. 6, 11127–11152. https://doi.org/10.3390/rs61111127.
- Taft, J.B., 1997. Savanna and open-woodland communities. In: Schwartz, M.W. (Ed.), Conservation in Highly Fragmented Landscapes. Springer New York, Boston, MA, pp. 24–54. https://doi.org/10.1007/978-1-4757-0656-7_2.
- US Geological Survey, 2019. Landsat 8 Surface Reflectance Code (LASRC) Product Guide (No. LSDS-1368).
- USDA Natural Resources Conservation Service, 2019. Gridded National Soil Survey Geographic Database (gNATSGO) [WWW Document]. URL. https://www.nrcs.usda.gov/wps/portal/nrcs/detail/soils/survey/geo/?cid=nrcseprd1464625 accessed 1.4.20.
- Van Gunst, K.J., Weisberg, P.J., Yang, J., Fan, Y., 2016. Do denser forests have greater risk of tree mortality: a remote sensing analysis of density-dependent forest mortality. Forest Ecology and Management, Special Section: Forests, Roots and Soil Carbon 359, 19–32. https://doi.org/10.1016/j.foreco.2015.09.032.
- Vermote, E., Justice, C., Claverie, M., Franch, B., 2016. Preliminary analysis of the performance of the Landsat 8/OLI land surface reflectance product. Remote sensing of environment. Landsat 8 Science Results 185, 46–56. https://doi.org/10.1016/j.rse. 2016.04.008.
- Waser, L.T., Küchler, M., Jütte, K., Stampfer, T., 2014. Evaluating the potential of WorldView-2 data to classify tree species and different levels of ash mortality. Remote Sens. 6, 4515–4545. https://doi.org/10.3390/rs6054515.
- Weiss, A., 2001. Topographic Position and Landforms Analysis, in: Poster Presentation. ESRI User Conference, San Diego, CA.
- Williams, A.P., Allen, C.D., Macalady, A.K., Griffin, D., Woodhouse, C.A., Meko, D.M., Swetnam, T.W., Rauscher, S.A., Seager, R., Grissino-Mayer, H.D., Dean, J.S., Cook, E.R., Gangodagamage, C., Cai, M., McDowell, N.G., 2013. Temperature as a potent driver of regional forest drought stress and tree mortality. Nat. Clim. Chang. 3, 292–297. https://doi.org/10.1038/nclimate1693.
- Zhen, Z., Quackenbush, L.J., Zhang, L., 2016. Trends in automatic individual tree crown detection and delineation—evolution of LiDAR data. Remote Sens. 8, 333. https:// doi.org/10.3390/rs8040333.